Chinese Chemical Letters 35 (2024) 109166

Contents lists available at ScienceDirect

Chinese Chemical Letters

journal homepage: www.elsevier.com/locate/cclet

Metal-encapsulated nitrogen-doped carbon nanotube arrays electrode for enhancing sulfion oxidation reaction and hydrogen evolution reaction by regulating of intermediate adsorption

Xiao Li[a,1], Wanqiang Yu[a,1], Yujie Wang[a,1], Ruiying Liu[a], Qingquan Yu[a], Riming Hu[b,*], Xuchuan Jiang[b], Qingsheng Gao[c], Hong Liu[a,d], Jiayuan Yu[a,*], Weijia Zhou[a,*]

[a] Institute for Advanced Interdisciplinary Research (iAIR), School of Chemistry and Chemical Engineering, University of Jinan, Ji'nan 250022, China
[b] Institute for Smart Materials & Engineering, School of Materials Science and Engineering, University of Jinan, Ji'nan 250022, China
[c] College of Chemistry and Materials Science, and Guangdong Provincial Key Laboratory of Functional Supramolecular Coordination Materials and Applications, Jinan University, Guangzhou 510632, China
[d] State Key Laboratory of Crystal Materials, Shandong University, Ji'nan 250100, China

ARTICLE INFO

Article history:
Received 1 June 2023
Revised 28 August 2023
Accepted 6 October 2023
Available online 8 October 2023

Keywords:
Sulfion oxidation reaction
Hydrogen evolution reaction
Nitrogen-doping carbon nanotube
Core-shell structure
Resource upgrade

ABSTRACT

For treatment of sulfion-containing wastewater, coupling the electrochemical sulfion oxidation reaction (SOR) with hydrogen evolution reaction (HER) can be an ideal way for sulfur and H_2 resources recovery. Herein, we synthesize a metal-modified carbon nanotube arrays electrode (Co@N–CNTs/CC) for SOR and HER. This electrode has excellent performance for SOR and HER attributed to the unique array structure. It can achieve 99.36 mA/cm^2 at 0.6 V for SOR, and 10 mA/cm^2 at 0.067 V for HER. Density functional theory calculations verify that metal modification is able to regulate the electronic structure of carbon nanotube, which is able to optimize the adsorption of intermediates. Employed Co@N–CNTs/CC as bifunctional electrodes to establish a hybrid electrolytic cell can reduce about 67% of energy consumption compared with the traditional water splitting electrolytic cell. Finally, the hybrid electrolytic cell is used to treat actual sulfion-containing wastewater, achieving the sulfur yield of 30 mg h^{-1} cm^{-2} and the hydrogen production of 0.64 mL/min.

Water pollution and energy crisis are one of the serious issues in current society [1–3]. Nowadays, large amount of sulfion-containing wastewater are produced during the industrial production, which has caused serious environmental pollution [4]. At present, the conventional methods for treatment those sulfion-containing wastewater include adsorption, membrane separation, biodegradation, *etc.* [5,6]. Although these methods are effective in purifying the polluted water, they do not recover the sulfur resources. In contrast to the above methods, ion exchange resin method can simultaneously purify water and recover sulfur resources, but limit by the high cost and complex process [7,8]. Hence, the development of new methods to recycle treatment the sulfion-containing wastewater is extremely important [9–12].

Hydrogen (H_2), as a kind of promising green energy, is brought about widespread attention. During water electrolysis, H_2 is produced at the cathode *via* a hydrogen evolution reaction (HER), and anodic oxygen evolution reaction (OER) occurs with a theoretical overall cell voltage of 1.23 V [13,14]. Regrettably, practical overall cell voltage is much higher than 1.23 V, owing to the sluggish anodic OER [15,16]. It is considered as an effective way to reduce the voltage of electrolytic cell by substituting the slow OER with the anodic oxidation reaction of other compounds, such as urea [17], alcohol [18], and hydrogen sulfide [19]. It is gratifying that sulfion oxidation reaction (SOR: $S^{2-} \rightarrow S + 2e^-$, $E = -0.48$ V *vs.* RHE) is more thermodynamically advantageous than that of OER ($E = 1.23$ V *vs.* RHE) [20]. There are many advantages if SOR is coupled with HER. (1) The driving voltage of this hybrid electrolytic cell will be greatly reduced to achieve H_2 production with low energy consumption. (2) The source of S^{2-} can be provided by the sulfion-containing wastewater. During the electrochemical oxidation process, not only the wastewater can be purified, but also the S^{2-} can be oxidated to S as a valuable chemical. However, compared with

* Corresponding authors.
E-mail addresses: ism_hurm@ujn.edu.cn (R. Hu), ifc_yujy@ujn.edu.cn (J. Yu), ifc_zhouwj@ujn.edu.cn (W. Zhou).
[1] These authors contributed equally to this work.

https://doi.org/10.1016/j.cclet.2023.109166
1001-8417/

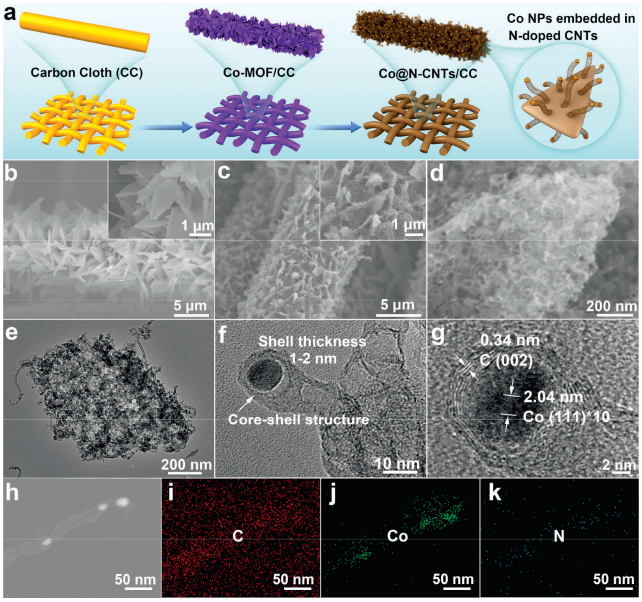

Fig. 1. (a) Preparation process of Co@N–CNTs/CC. (b) FESEM image of Co-MOF/CC. (c, d) FESEM, (e, f) TEM, (g) HRTEM, (h) STEM images and (i-k) according C, Co, N elemental mapping of Co@N–CNTs/CC.

the extensive exploration of HER electrocatalysts [21], the high-efficient and long-term stable electrocatalyst on SOR is still insufficient.

Metal-based electrocatalysts have been proved with high catalytic performance for SOR [22–26]. However, the exposed of active substance metals are susceptible to corrosion or poisoning by S^{2-} leading to activity and stability decrease. Hence, developing high catalytic activity and stable electrocatalysts is essential to achieve sustainable SOR. Our previous work confirmed that coating of carbon shell can effectively protect the metal-based catalyst from etching [27]. At the same time, the electron transfer between the inner metal and the carbon shell is conducive to enhancing electrocatalytic activity [28,29]. In addition, more active sites can be exposed with the increasing of the specific surface area by building a whole array of nanowires [30,31], nano sheets [32,33], nanotubes [34,35], *etc.*, which is conducive to improve catalytic activity.

Bearing these points in mind, we put forward a self-template growth method for preparing a nitrogen-doped carbon nanotube arrays encapsulating with cobalt nanoparticle on carbon cloth (Co@N–CNTs/CC) as the effective electrode for simultaneous sulfur recycling and hydrogen generation from sulfion-containing wastewater. The as-prepared Co@N–CNTs/CC showed excellent performance compared to RuO_2 and possessed long-term durability over 120 h. Meanwhile, the Co@N–CNTs/CC electrode also exhibited excellent performance toward HER. Theory calculations demonstrated that the unique core-shell structure of Co@N–CNTs could promote the adsorption of intermediates on carbon surface, therefore resulting in high SOR and HER performances.

The dendrites-like electrocatalyst, nitrogen-doped carbon nanotubes micro-nano array encapsulated with cobalt nanoparticle on carbon cloth (Co@N–CNTs/CC), was prepared *via* a self-template growth method (Fig. 1a). First of all, the O_2-plasma treated hydrophilic carbon cloth (Fig. S1 in Suppporting information) was employed as flexible substrate for the growth of microsheet-like metal-organic frameworks (Co-MOF/CC, Fig. 1b and Fig. S2 in Supporting information) arrays *via* a facile room-temperature crystallization route [36–38]. During this process, the treatment of O_2-plasma is crucial for the full growth of Co MOF (Fig. S3 in Supporting information). In the second step, the Co-MOF was *in-situ* transformed to hierarchical Co@N–CNTs array by pyrolysis with dicyandiamide at 800 °C. After pickling treatment to remove the uncoated Co NPs in Co@N–CNTs/CC, the final product was obtained.

In the process of synthesis, the calcination temperature and the amount of dicyandiamide have a great influence on the morphology, and then affect the performance (Figs. S4–S7 in Suppporting information). The detailed morphology and structure evolution of the optimal Co@N–CNTs/CC was firstly analyzed by field emission scanning electron microscope (FESEM) and transmission electron microscope (TEM). The surface of carbon micro-sheets was growth numerous Co@N–CNTs (Figs. 1c and d), which were about 20 nm in diameter and hundreds of nanometers to micrometers in length. For further characteristic the microstructure of Co@N–CNTs, the sample was peeled up from the CC and then measured by TEM. As depicted in Figs. 1e and f, it could be clearly found that abundant of nanoparticles, speculated as metallic Co, with the size of 5–10 nm were captured in the top of the carbon nanotube (CNTs). To verify this guess, the high-resolution TEM (HRTEM) measurement was employed. As shown in Fig. 1g, the lattice fringes with interplanar spacing distances of 0.204 and 0.34 nm were in good accordance with the metal Co (111) and graphite C (200) planes, respectively. Additionally, the hierarchical carbon dendrite feature in the typical morphology of Co@N–CNTs was verified through the scanning transmission electron microscopy (STEM) and elemental mapping. Elemental mapping images (Figs. 1h–k) of a single Co@N–CNT exhibited the core-shell structure of Co nanoparticle encapsulated in the top of N-doped CNTs. All the above results confirmed that Co@N–CNTs/CC was successfully prepared.

The crystal phase of Co@N–CNTs/CC was identified by the X-ray diffraction (XRD) pattern (Fig. 2a). Metal Co phases with the diffraction peaks at 44.2° (111), 51.5° (200), and 75.8° (210) were confirmed in Co@N–CNTs/CC (JPCDS No. 15-0806). The broad diffraction peaks at 26.6° were assigned to carbon indicating the defect-rich nature [39,40]. To further study the characteristic of C in Co@N–CNTs/CC, Raman spectrum (Fig. 2b) was measured. The peaks of 1360 cm^{-1} (D band), 1591 cm^{-1} (G band), and 2700 cm^{-1} (2D band) were appeared. High I_D/I_G band intensity ratio of Co@N–CNTs/CC demonstrated plenty of N atoms doping in graphite carbon layer to form rich defects. Moreover, the shape and weak intensity of 2D band demonstrated the existence of multilayers graphene in Co@N–CNTs/CC, and consistent with the structure in Fig. 1g. Surface area (S_{BET}) and porosity of Co@N–CNTs/CC were studies through nitrogen adsorption-desorption isotherms. The curve could be divided into two parts, rapid absorption at low relative pressure (<0.05) and gradual absorption at high relative pressure (0.45–1.0) with hysteresis loop (Fig. 2c). The result indicated that micropores and mesopores were coexistent, which was confirmed in pore size distributions (inset in Fig. 2c). S_{BET} and pore volume of Co@N–CNTs/CC was 330.8 m^2/g and 0.263 cm^3/g. Higher S_{BET} of electrode facilitated to provide more active sites.

Surface chemical composition and electronic states of Co@N–CNTs/CC was investigated by X-ray photoelectron spectroscopy (XPS). The C, N, Co, and O elements existed in full XPS spectrum (Fig. S8 in Supporting information). Co 2p XPS spectrum (Fig. 2d) showed that the peaks at 780.7 and 796.0 eV could be corresponding to Co^{2+} $2p_{3/2}$ and Co^{2+} $2p_{1/2}$. Meantime, the peaks at 778.5 and 795.7 eV revealed the present of Co^0 in sample [41–43]. For C 1s spectrum, the fitted C 1s XPS spectrum (Fig. 2e) showed two main peaks near 284.8 and 285.5 eV, corresponding to sp^2 carbon and C–N species, respectively. High-resolution N 1s XPS spectrum (Fig. 2f) was analyzed to study the type of N species in Co@N–CNTs/CC. Three peaks at 398.7, 399.8, and 401.3 eV were assigned to pyridinic N, pyrrolic N, and graphitic N, respectively.

Valence states and coordination environment of cobalt species can be further analyzed by X-ray absorption fine structure spec-

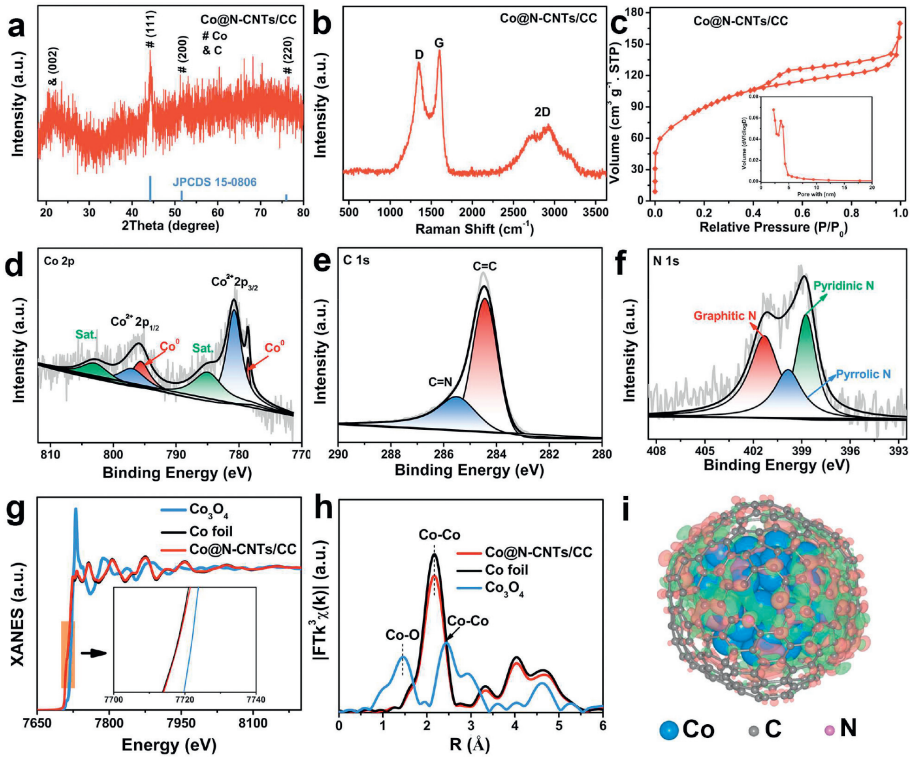

Fig. 2. (a) XRD, (b) Raman spectrum and (c) N_2 adsorption-desorption isotherms of Co@N–CNTs/CC. High-resolution XPS spectra of Co@N–CNTs/CC of (d) Co 2p, (e) C 1s, and (f) N 1s. (g) XANES and (h) Co K-edge FTEXAFS spectra of Co@N–CNTs/CC, Co_3O_4 and Co foil. (i) Calculated charge-density differences of Co@N–CNTs/CC, red (green) represents the charge accumulation (deletion).

trum. Fig. 2g shown that the valence state of Co in Co@N–CNTs/CC was slightly larger than that of Co foil. In Fig. 2h, only one peak at 2.17 Å assigned to Co-Co bond was observed in the curve of Co@N–CNTs/CC, indicating that there was no oxidation exist in the sample. These results indicated that the increase in the valence state of cobalt species is caused by the transfer of electrons from the metal core to the carbon shell. At the same time, this charge transfer phenomenon is confirmed by charge-density differences of Co_{55}@N–C_{240}. An obvious charge transfer behavior from Co_{55} cluster to the shell of N–C_{240} could be observed, which leaded to the enrichment of charge density on N–C_{240} shell (Fig. 2i).

Electrochemical tests were conducted on the electrocatalytic SOR and HER performance of Co@N–CNTs/CC using a system of three electrodes. First of all, the polarization curves were measured in 1 mol/L NaOH containing 1 mol/L Na_2S. The Co@N–CNTs/CC exhibited an excellent SOR activity with lower onset potential (0.217 V) than those of the Co NPs, N–CNTs, 20 wt% Pt/C, RuO_2. The overpotential of Co@N–CNTs/CC was 0.28 V to achieve 10 mA/cm^2 (Fig. 3a). The current density of different electrodes at 0.4, 0.5, and 0.6 V were summarized in Fig. 3b. The current density of Co@N–CNTs/CC could reach up to 99.36 mA/cm^2 at 0.6 V, which was 5.8 and 3.3 times higher than those of 20 wt% Pt/C (17.26 mA/cm^2) and RuO_2 (30.28 mA/cm^2), respectively. The electrocatalytic kinetics of SOR was investigated by electrochemical impedance spectroscopy. The charge transfer resistance of Co@N–CNTs/CC was smaller than those of Co NPs, N–CNTs, 20 wt% Pt/C and RuO_2 at 0.4 V *vs.* RHE (Fig. 3c), indicating that Co@N–CNTs/CC owned faster electron transfer rates. The quantity of active sites on electrodes were qualitative by electrochemically active surface area (ECSA). ECSA of Co@N–CNTs/CC was 14.22 mF/cm^2 (Fig. 3d and Fig. S9 in Supporting information), which was much higher than that of Co NPs (2.21 mF/cm^2), N–CNTs (3.17 mF/cm^2), 20 wt% Pt/C (1.76 mF/cm^2) and RuO_2 (5.73 mF/cm^2). High ECSA was crucial to obtain high current density for SOR. However, after correlation between the LSV and ECSA of the samples, the Co@N–CNTs/CC catalyst still exhibited the highest activity. This result indicated that constructing a core-shell structure can effectively enhance the intrinsic activity of the catalyst and expose more active sites (Fig. S10 in Supporting information). Besides, the current density of Co@N–CNTs/CC maintained at around 100 mA/cm^2 (Fig. S11a in Supporting information) in 120 h at 0.65 V *vs.* RHE. After 120 h durability test, the polarization curve showed almost exactly the same as initial performance (Fig. S11b in Supporting information) and the structure of Co@N–CNTs/CC has not undergone significant changes (Fig. S12 in Supporting information), indicating the outstanding durability of Co@N–CNTs/CC. All above results demonstrated the high SOR performance of Co@N–CNTs/CC.

Electrocatalytic OER and HER performance of Co@N–CNTs/CC were assessed by the polarization curves in 1 mol/L NaOH. In Fig. 3e, it needed 1.37 V to achieve 10 mA/cm^2 for OER, which was larger than that of SOR (0.28 V). This result indicated that the energy consumption could be significantly reduced by replacing OER with SOR. Furthermore, the Co@N–CNTs/CC exhibited superior HER activity, which only needed the overpotential of 0.067 V to achieve 10 mA/cm^2. For the sake of analyzing kinetics of HER, the according Tafel slopes (Fig. S13 in Supporting information) were gained *via* the equation of $\eta = a + b\log|j|$. The values of all the samples exceeded than 120 mV/dec, indicating rate-limiting step of the HER is Volmer step. Generally, the current density of HER would be associated with the quantity of electrocatalytic active site, which was calculated by the double layer capacitance (Figs. S14 and S15 in Supporting information). ECSA of Co@N–CNTs/CC was 107.0 mF/cm^2, which was larger than that of Co NPs (5.17 mF/cm^2), N–CNTs (15.58 mF/cm^2) and 20 wt% Pt/C (29.14 mF/cm^2). Usually, larger ECSA provided more active sites achieving higher current

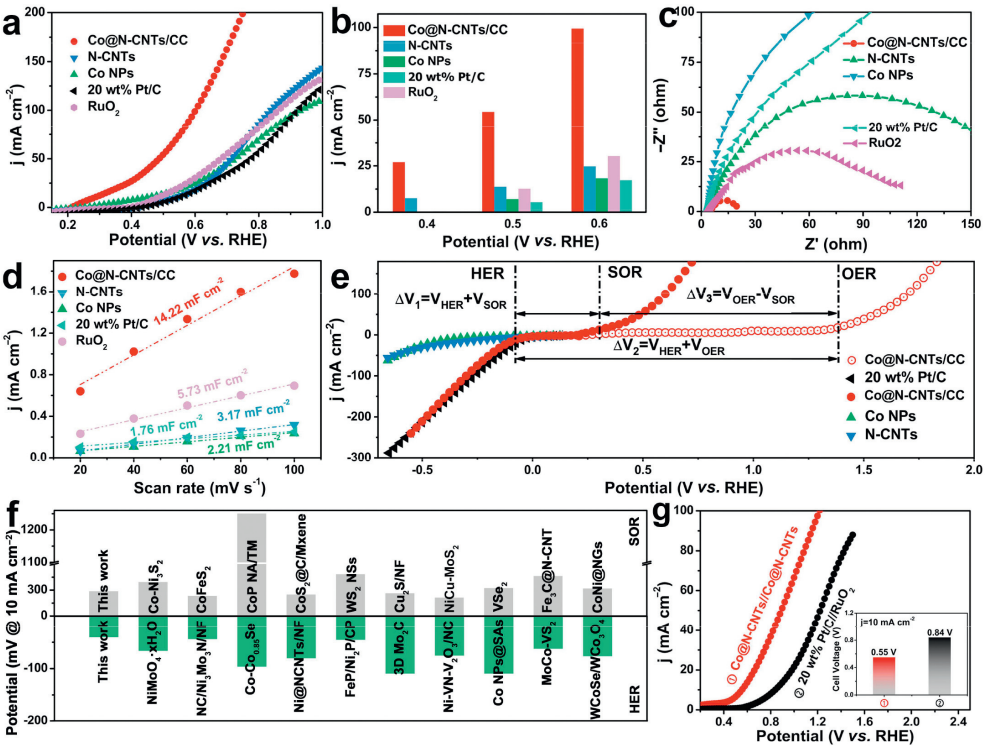

Fig. 3. (a) SOR polarization curves and (b) current densities at the potentials of 0.4, 0.5 and 0.6 V for samples. (c) Nyquist curves of samples tested at 0.4 V. (d) The capacitive currents as a function of scan rates. (e) LSV of as-prepared Co@N–CNTs/CC in comparison with contrast materials, and SOR and OER polarization curves of Co@N–CNTs/CC. (f) Comparison of the SOR and HER performance with reported literatures. (g) LSV of (+)Co@N–CNTs||Co@N–CNTs(−) and (+)Pt/C||RuO_2(−) in the hybrid electrolytic cell of coupling SOR with HER.

density. Furthermore, the durability measurements confirmed that the integrated Co@N–CNTs/CC had robust stability (Figs. S16–S18 in Supporting information). Actually, the Co@N–CNTs/CC showed superior activities for SOR and HER to most of the previously reported nonprecious metal base electrocatalysts (Fig. 3f, Tables S1 and S2 in Supporting information).

To obtain high energy conversion efficiency of electrolytic water, a fast kinetic SOR was adopted to instead of the slow kinetic OER. A homemade coupled electrolyzer system of HER with SOR by using Co@N–CNTs/CC as cathode and anode produced H_2 and upcycled S^{2-} to S, respectively. As illustrated in Fig. 3g, the overpotential of electrolyzer was 0.55 V to afford 10 mA/cm^2 for HER(−)//SOR(+), which was smaller than 0.84 V in 20 wt% Pt/C(−)//RuO_2(+) electrolyzer.

To gain further understand the source of high performance of Co@N–CNTs/CC, Density functional theory (DFT) calculations were performed. According to structural characteristics of Co@N–CNTs/CC, the core@shell structure of a carbon cage (C_{240}) encapsulated 55 metal atoms cluster (Co_{55}) was constructed, which worked well in previous studies [44–49]. In addition, to clarify the effect of doping N element, it was created in C_{240}. As a result, a total of three structures, including C_{240}, Co@C_{240} and Co@N–C_{240} were employed in this work (Fig. 4a).

Firstly, the catalytic performances towards SOR of different models were evaluated and the catalytic reaction pathways (S^{2-} to S_4) of CNTs/CC, Co@CNTs/CC and Co@N–CNTs/CC were confirmed by ultraviolet and visible (UV–vis) spectrophotometry system (Fig. S19 in Supporting information). According to the computational results as shown in Fig. 4b, the adsorption and activation of intermediate S* state on C_{240} was relatively difficult due to their high ΔG from S^{2-} to S* (ΔG_1), which seriously hindered the progress of the SOR. As for Co@C_{240} and Co@N–C_{240}, the ΔG_1 was significantly reduced. The results indicated that the internal metal can greatly optimize the intermediates adsorption of carbon shell. And the potential-determining steps (PDS) of Co@N–C_{240} was also changed from the first step to the third step. Projected density of states (PDOS) in Fig. 4c showed a downshifted band center for the occupied state of the S-N bond on Co@N–C_{240} compared with S-C on C_{240}. Meanwhile, the hybridized peaks (located at around −1.2 and −3.2 eV) between N-2s and S-3p orbitals could be observed. These revealed that the stronger S-C chemical bonding enhanced the sulfur adsorption on Co@N–C_{240} to enhance the SOR activity.

As for HER, the adsorption free energy of H* (ΔG_{H^*}) on different models were calculated. Fig. 4d showed the calculated ΔG_{H^*}. A higher value of ΔG_{H^*} was observed for C_{240}, indicating its low HER activity. Interestingly, ΔG_{H^*} was significantly reduced from 1.22 eV to 0.61 eV by encapsulating Co_{55} core, and the introduction of N atom could further optimize ΔG_{H^*}. The value of ΔG_{H^*} closed to 0 eV for Co@ N–C_{240} ($\Delta G_{H^*} = -0.18$ eV), indicated their excellent catalytic activity for HER, which was consistent with our experimental results.

To determine the effectiveness of the above hybrid electrolytic cell system to utilize sulfion-containing wastewater for production of sulfur and H_2 in a realistic system, a demo was constructed for electrocatalytic selective removal of H_2S from simulated industrial syngas (V_{CO}:V_{H_2} = 1:1, with 2% H_2S), which employed Co@N–CNTs/CC as a bifunctional electrode (Fig. 5a). Compared with traditional treatment methods, electrochemical methods were cleaner, more efficient and had mild reaction conditions. In order to verify the ability of 1 mol/L NaOH electrolyte to remove H_2S impurities in the synthesis gas, we tested the content of H_2S in the synthesis gas after flowing through the electrolyte in different times. As shown in Fig. 5b, the analysis result of gas chromatography showed that the impurity content of H_2S in the synthesis gas could be almost ignored after purification in the electrolytic cell. Polarization curves showed that the

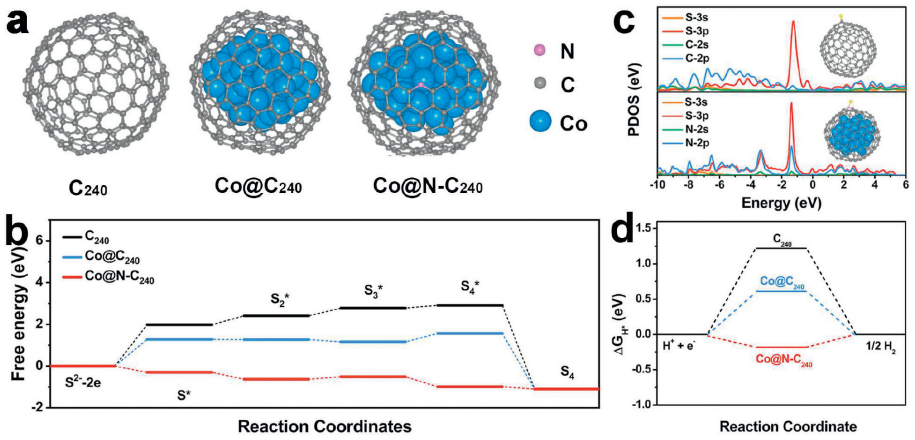

Fig. 4. (a) Structural diagrams of C_{240}, Co@C_{240}, and Co@N–C_{240}. (b) Calculated SOR free energy diagram on different models. (c) Comparison of PDOS of S(3s3p) and its bonded C(2s2p) or N(2s2p) when S is adsorbed on C_{240} and Co@pyridinic N–C_{240}. (d) Calculated adsorption free energy of H* (ΔG_{H^*}) on different models.

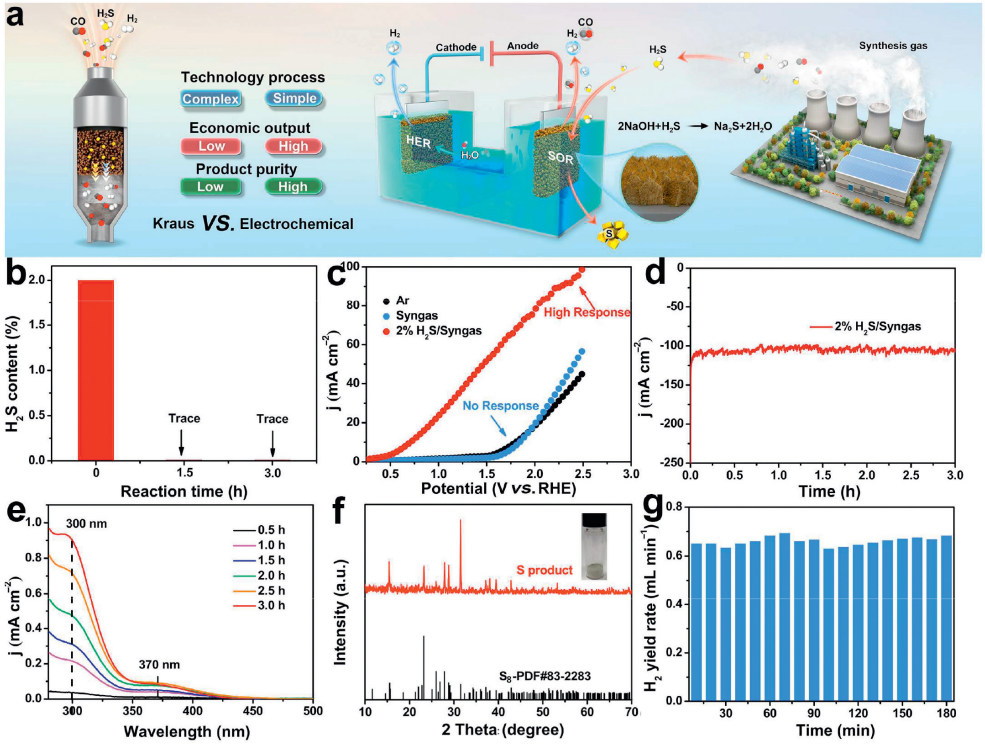

Fig. 5. (a) The schematic diagram of a demo for the selective removal of H_2S from industrial syngas and produce H_2 employed Co@N–CNTs/CC as cathode and anode in 1 mol/L NaOH. (b) Hydrogen sulfide content in synthesis gas after flowing through electrolytic cell at different times. (c) The polarization curves for the activity over (-)Co@N–CNTs/CC//Co@N–CNTs/CC(+) in industrial syngas (V_{CO}:V_{H_2} = 1:1, with 2% H_2S), syngas (V_{CO}:V_{H_2} = 1:1) and Ar. (d) *i-t* curve of (-)Co@N–CNTs/CC//Co@N–CNTs/CC(+) for removing H_2S in industrial syngas accompanying HER. (e) UV–vis spectra of electrolytes in a galvanostatic test. (f) XRD pattern of product sulfur. Inset: photo of collected sulfur powder. (g) The yield rates of H_2 production.

(-)Co@N–CNTs/CC//Co@N–CNTs/CC(+) electrolyzer system showed obvious response current when containing 2% H_2S in syngas, while hardly any response for syngas without H_2S (Fig. 5c). This indicated that Co@N–CNTs/CC owned excellent activity for the selective oxidation of S^{2-}, while CO and H_2 would not be spent in purification process.

To obtain actual yield of electrolyzer system of (-)Co@N–CNTs/CC//Co@N–CNTs/CC(+) for oxidation of S^{2-} and production of H_2, a galvanostatic test at 100 mA/cm^2 was carried out (Fig. 5d). At the anode, the oxidation product was tested by visible (UV–vis) spectrophotometry system [50,51]. The peaks at 300 and 370 nm represented short-chain polysulfides (S_2^{2-}–S_4^{2-}) in the electrolyte (Fig. 5e). With the progress of the reaction, the signal intensity of polysulfide increased significantly. The polysulfides could be converted into yellow powders by further acid treatment [44]. The obtained powder was confirmed to be elemental sulfur by XRD analysis (Fig. 5f). After calculation, the production rate of sulfur reached 30 mg h^{-1} cm^{-2}. At the cathode, profiting from the excellent catalytic activity of the Co@N–CNTs/CC for HER. Through real-time monitoring by gas chromatography, H_2 production was kept at about 0.64 mL/min (Fig. 5g). These results demonstrated that the Co@N–CNTs/CC electrocatalyst could effectively eliminate H_2S impurities from industrial syngas, and produced of H_2 and S, synchronously. In order to further explore the stability of the above hybrid electrolytic cell system, we extended the test time to 72 h (Fig. S20

in Supporting information). It was apparently that the obvious declined current density was not observed. Therefore, the stability of the (-)Co@N–CNTs/CC//Co@N–CNTs/CC(+) electrolyzer system was outstanding.

In summary, we constructed a dendritic core-shell structure catalyst *via* a self-template growth method to prepare a Co nanoparticle encapsulated within a nitrogen-doped CNTs loaded on carbon cloth. The core-shell catalyst possessed an ultralow overpotential (0.28 V) to afford 10 mA/cm^2 for SOR. The current density of the catalyst was 3.28 times higher than that of RuO_2 at 0.6 V. The optimized electrode owned outstanding durability for 120 h. Meanwhile, Co@N–CNTs/CC exhibited high performance of HER with a low overpotential of 67 mV to achieve 10 mA/cm^2. DFT calculations indicated that excellent activity for SOR and HER might attribute to the modulation of surface electronic structure of graphene by encapsulating a Co nanoparticle and doping with nitrogen, which facilitated the adsorption of the intermediates on the surface of graphene. Finally, the electrolytic cell was used to treat actual sulfion-containing wastewater, achieving the hydrogen production of 0.64 mL/min and the sulfur yield of 30 mg h^{-1} cm^{-2}. This study shows a novel scheme to recover and utilize sulfion-containing wastewater.

Declaration of competing interest

The authors declare that they have no known competing financial interests or personal relationships that could have appeared to influence the work reported in this paper.

Acknowledgments

This work was supported by Natural Science Foundation of Shandong Province (Nos. ZR2022QE076, ZR2021JQ15, ZR2019YQ20), the National Natural Science Foundation of China (Nos. 52002145, 52202092, 51972147, 52022037) and Taishan Scholars Project Special Funds (No. tsqn201812083). The authors thank the photoemission endstations BL1W1B in Beijing Synchrotron Radiation Facility (BSRF).

Supplementary materials

Supplementary material associated with this article can be found, in the online version, at doi:10.1016/j.cclet.2023.109166.

References

[1] J. Du, D. Xiang, K. Zhou, et al., Nano Energy 104 (2022) 107875.
[2] Y. Chen, Y. Wang, J. Yu, et al., Adv. Sci. 9 (2022) e2105869.
[3] J. Yu, W. Yu, B. Chang, et al., Chin. Chem. Lett. 33 (2022) 3231–3235.
[4] X. Zhang, R. Qi, A. Wu, et al., Chem. Eng. J. 427 (2022) 130963.
[5] M. Shah, M. Tsapatsis, J. Siepmann, Chem. Rev. 117 (2017) 9755–9803.
[6] X. Yao, Y. Shi, K. Wang, et al., Sci. Total Environ. 808 (2022) 152130.
[7] L. Prochnow, F. Pismel, H. Cantarella, et al., Commun. Soil. Sci. Plant Anal. 29 (2008) 1833–1841.
[8] G. Lei, Y. Tong, L. Shen, et al., Small 16 (2020) e2003904.
[9] S. Hao, L. Yang, D. Liu, et al., Int. J. Hydrog. Energy 42 (2017) 26289–26295.
[10] M. Kumar, T. Nagaiah, J. Mater. Chem. A 10 (2022) 7048–7057.
[11] S. Han, M. Zhang, Z. Fu, et al., Adv. Mater. 34 (2022) e2202830.
[12] Y. Li, Y. Duan, K. Zhang, et al., Chem. Eng. J. 433 (2022) 134472.
[13] Y. Zeng, M. Zhao, Z. Huang, et al., Adv. Energy Mater. 12 (2022) 2201713.
[14] D. Jiang, L. Yang, H. Yuan, et al., Nano Energy 93 (2022) 106892.
[15] X. Qiao, X. Yin, L. Wen, et al., Chem 8 (2022) 3241–3251.
[16] J. He, F. Liu, Y. Chen, et al., Chem. Eng. J. 432 (2022) 134331.
[17] J. Li, Y. Li, Q. Xue, et al., Chin. J. Struct. Chem. 41 (2022) 2207035–2207039.
[18] Q. Xue, Z. Xia, W. Gou, et al., ACS Catal. 13 (2023) 400–406.
[19] L. Yi, Y. Ji, P. Shao, et al., Angew. Chem. Int. Ed. 60 (2021) 21550–21557.
[20] L. Zhang, Z. Wang, J. Qiu, Adv. Mater. 34 (2022) e2109321.
[21] J. Yu, W. Yu, Y. Wang, et al., Chem. Eng. J. 433 (2022) 134553.
[22] L. Su, A. Badel, C. Cao, et al., Ind. Eng. Chem. Res. 56 (2017) 9783–9792.
[23] I. Pikaar, R. Rozendal, Z. Yuan, et al., Water Res. 45 (2011) 5381–5388.
[24] W. Feng, M. Cheng, R. Du, et al., Adv. Mater. Interfaces 9 (2022) 2200060.
[25] D. Zhao, Y. Wang, C. Dong, et al., Nano Micro Lett. 14 (2022) 223.
[26] K. Petrov, S. Srinivasan, Int. J. Hydrog. Energy 21 (1996) 163–169.
[27] W. Yu, J. Yu, Y. Wang, et al., Appl. Catal. B: Environ. 310 (2022) 121291.
[28] S. Xie, H. Jin, C. Wang, et al., Chin. Chem. Lett. 34 (2022) 107681.
[29] X. Li, Z. Wang, Y. Tian, et al., Chin. Chem. Lett. 34 (2022) 107812.
[30] J. Deng, Y. Su, D. Liu, et al., Chem. Rev. 119 (2019) 9221–9259.
[31] U. Ali, H. Yang, V. Khayrudinov, et al., Small 18 (2022) 2201968.
[32] S. Venkateswarlu, H. Mahajan, A. Panda, et al., Chem. Eng. J. 420 (2021) 127584.
[33] H. Chen, Z. Shen, Z. Pan, et al., Adv. Sci. 6 (2019) 1802002.
[34] N. Wang, R. Zheng, T. Chi, et al., Compos. B Eng. 239 (2022) 109952.
[35] J. Ackermann, J. Metternich, S. Herbertz, et al., Angew. Chem. Int. Ed. 61 (2022) e202112372.
[36] C. Guan, X. Liu, W. Ren, et al., Adv. Energy Mater. 7 (2017) 1602391.
[37] G. Fang, J. Zhou, C. Liang, et al., Nano Energy 26 (2016) 57–65.
[38] R. Chen, J. Yao, Q. Gu, et al., Chem. Commun. 49 (2013) 9500–9502.
[39] Y. Li, X. Wang, M. Sun, et al., ACS Nano 16 (2022) 17008–17020.
[40] X. Cheng, J. He, H. Ji, et al., Adv. Mater. 34 (2022) 2205767.
[41] X. Yu, B. He, W. Li, et al., J. Mater. Chem. A 10 (2022) 12168–12176.
[42] R. Wang, K. Lu, J. Zhang, et al., ACS Catal. 12 (2022) 14290–14303.
[43] Y. Pan, X. Wang, W. Zhang, et al., Nat. Commun. 13 (2022) 3063.
[44] M. Zhang, J. Guan, Y. Tu, et al., Energy Environ. Sci. 13 (2020) 119–126.
[45] Y. Tu, P. Ren, D. Deng, et al., Nano Energy 52 (2018) 494–500.
[46] X. Cui, P. Ren, D. Deng, et al., Energy Environ. Sci. 9 (2016) 123–129.
[47] J. Deng, P. Ren, D. Deng, et al., Angew. Chem. Int. Ed. 54 (2015) 2100–2104.
[48] X. Hu, G. Wang, J. Li, et al., Energy Environ. Sci. 14 (2021) 4564–4573.
[49] Q. Yang, P. Jin, B. Liu, et al., J. Mater. Chem. A 8 (2020) 9049–9057.
[50] Y. Wu, N. Liu, Chem 4 (2018) 438–465.
[51] C. Barchasz, F. Molton, C. Duboc, et al., Anal. Chem. 84 (2012) 3973–3980.